### ORIGINAL RESEARCH ARTICLE



# Influence of Crystallographic Orientation on the Deformation of Ag Nanoparticles During High-Speed Impact

T. V. Chitrakar<sup>1</sup> · Michael F. Becker<sup>1,2,4</sup> · Desiderio Kovar<sup>1,3,4</sup>

Submitted: 18 April 2023/in revised form: 1 September 2023/Accepted: 17 September 2023/Published online: 27 September 2023 © ASM International 2023

Abstract Several related aerosol processes utilize a supersonic gas jet to impact solid nanoparticles to produce nanograined films. Although the influence of important control variables such as particle size and particle impact velocity on particle deformation and film formation for these processes have been previously studied, other variables have not been systematically explored. One parameter that cannot be controlled in experiments is the particle impact orientation. Because particles impact with a full range of crystallographic orientations, an understanding of the effect of particle orientation is required to predict film microstructures. In this study, molecular dynamics simulations were conducted with Ag to determine the influence of particle crystallographic orientation on the deformation experienced by the particle upon impact and the resulting microstructure of the deposit. It is shown that the orientations that produce the largest overall particle deformation are not correlated to orientations where the initiation of plastic deformation is easiest, as one might expect. Rather, the deformation experienced by the particle is heterogeneous and depends on the mechanisms responsible for deformation. Two deformation mechanisms are identified:

(1) dislocation plasticity and (2) disordering followed by viscous flow. The fraction of the atoms in the impacting particle that experience deformation by each mechanism is quantified as a function of particle orientation. The implications of the effects of particle crystallographic orientation on film microstructures are also discussed.

**Keywords** aerosol nanoparticle deposition · molecular dynamics · particle impact deformation · silver nanoparticles

## Introduction

Thick films of metals and ceramics can be produced by high velocity impact of solid nanoparticles (NPs or ultrafine particles) onto substrates using a supersonic gas jet. Films have been produced by deposition of NPs with diameters < 70 nm formed by evaporation/condensation (Ref 1, 2) and of NPs < 20 nm by the laser ablation of microparticle aerosols (LAMA) (Ref 3-6). Both processes can produce unagglomerated nanoparticles; evaporation/condensation does so when operated at low particle densities, whereas charging of the nanoparticles that occurs during the laser ablation process prevents agglomeration in the LAMA process. These processes have been used to produce patterned, thick, electrically conductive metal films (Ref 2, 5, 7). However, in these experiments, the impacting particle orientation was not and could not be controlled, and for near-spherical particles, random impact orientations are expected. Simulations are thus necessary to discern orientation differences in the deposition process.

The fine particle sizes combined with very high-impact velocities used in aerosol jet deposition of ultrafine nanoparticles does not allow direct imaging at time or



Michael F. Becker mfbecker@austin.utexas.edu

Materials Science and Engineering Program and Texas Materials Institute, The University of Texas at Austin, Austin, TX 78712, USA

Department of Electrical and Computer Engineering, The University of Texas at Austin, Austin, TX 78712, USA

Department of Mechanical Engineering, The University of Texas at Austin, Austin, TX 78712, USA

Center for Additive Manufacturing and Design Innovation, The University of Texas at Austin, Austin, TX 78712, USA

spatial scales sufficient to resolve relevant phenomena that occur during particle impact. Molecular dynamics (MD) simulations have been used to study particle impact events because of their ability to resolve features down to the atomic level with sub-picosecond resolution. (Ref 8-12) However, the significant computational expense for these simulations typically limits studies to individual particles with diameters < 50 nm, which is particularly suitable for simulating aerosol deposition of NPs produced by the evaporation/condensation and LAMA processes described above. MD simulations have proven to be invaluable to identifying mechanisms for particle deformation and sticking. The film microstructure, including porosity, grain orientations, and grain size, is determined by the mechanisms of particle deformation that occur upon impact. These characteristics in turn affect properties such as the mechanical behavior, adhesion, and the electrical and thermal conductivities of the resulting films.

A previous study reported the deformation mechanisms and resulting film microstructures that occur upon particle impact using MD simulations for a range of Ag NP sizes (2-9 nm) and impact velocities (10-1500 m/s). (Ref 13) For these simulations, a single particle orientation was considered with the particle oriented with the [001] direction along the impact axis, and the substrate oriented with the same orientation as the particle, except it was rotated about the impact axis by 45° so that the lattices of the particle and substrate were not commensurate. It was shown that at low impact velocities, the deformation experienced by the particles was governed by dislocation emission from the particle-substrate contact region. Subsequent dislocation propagation resulted in dislocation-dislocation interactions that lead to heterogeneous deformation in the particle. The same mechanism was also observed at higher velocities, but the higher strain rate and increased strain magnitude resulted in a nearly complete disordering of the impacting NP. When the particle bonded to the substrate, a wide range of final states were observed that depended on the NP size and impact velocity. These final states ranged from polycrystalline to epitaxial containing several defects. In another study, a similar range of final states ranging from polycrystalline to epitaxial were observed experimentally using TEM for nominally similar particle sizes (5-30 nm) and impact velocities (< 900 m/s). These results suggest that particle size and particle impact velocity are not the only parameters that influence final morphologies. (Ref 14) This study also suggests that, because the particle impact orientation varies from particle-to-particle, orientation is an additional variable that could affect particle deformation.

Our focus in this paper is to determine if there is a particle orientation dependence for particle sizes and velocities relevant to metal film deposition from ultrafine nanoparticle aerosols, and if so, to study possible deformation mechanisms that can lead to particle sticking. In particular, we would like to answer the question, do orientation effects persist as NP size and velocity increase? Accordingly, we use MD simulations to study the impact of Ag NPs (4.5-9 nm diameter and 300-1500 m/s) over a large range of crystal orientations onto a substrate with a fixed crystal orientation. A fixed orientation for the substrate is used because preliminary studies indicated that the orientation of the impacting particle plays larger role on the particle deformation compared to the substrate orientation. At the smaller NP sizes and modest impact velocities, both dislocation plasticity and disordering mechanisms are active in this regime, and these two mechanisms have been shown to be the primary deformation mechanisms that are relevant for aerosol deposition processes.

Schmid factor analysis is the traditional tool used to predict the influence of orientation on onset of plastic deformation in crystals. (Ref 15) Thus, it is first hypothesized that there should be a correlation between the total deformation experienced by NPs upon impact and the theoretically calculated Schmid factors. However, the simulations we subsequently report here suggest that a Schmid factor analysis cannot predict the observed trends, and that an understanding of the underlying deformation mechanisms is required to explain the orientation dependence on the deformation. Additional simulations are conducted for NP orientations where maximum and minimum deformation is observed to study the underlying deformation mechanisms and to characterize the influence of particle orientation on the deformation experienced by the impacting particle for a range of particle sizes and velocities that encompass experimental film deposition parameters.

#### Methods

Molecular dynamics (MD) simulations were conducted using LAMMPS (Ref 16) running on the Lonestar6 Linux cluster at the Texas Advanced Computing Center (TACC) at the University of Texas at Austin to study the influence of crystallographic orientations on deformation mechanisms when Ag NPs impact onto a stationary Ag substrate. The Ag interatomic interaction was described by the embedded-atom-method (EAM) potential (Ref 17) downloaded from the NIST Interatomic Potentials Project. The simulation volume was  $60 \times 60 \times 80$  lattice constants (LC = 0.409 nm for Ag) with periodic boundary conditions applied in all three dimensions of the simulation volume. The substrate is present in the bottom portion of the simulation volume ( $60 \times 60 \times 40$  LC). The lower 5 LC of the substrate was held at 300 K to simulate the heat sink of a



semi-infinite substrate, and the next lower 5-10 LC was a 300 K Langevin sink to damp acoustic waves.

Spherical, defect-free NPs with diameters of 4.5, 6 and 9 nm were impacted at velocities between 300 and 1500 m/s onto a flat substrate that had a fixed crystallographic orientation with Miller indices of x [100], y [010], z [001]. The impacting orientations of the particles were systematically varied to assess the influence of particle orientation on deformation following impact. At the start of each simulation, the center of the impacting NP was placed above the substrate so that it did not touch either the substrate or the simulation box boundary, which was equivalent to the NP floating in vacuum. Before the NP was set in motion in the -z direction, the whole system was thermalized at 300 K for 40 ps. This temperature is consistent with the nominal experimental conditions used to impact NPs (Ref 5) via the LAMA process. To prevent undesirable NP rotations during thermalization, the angular momentum of the NP was zeroed at every time-step during thermalization. The NP-substrate system was prevented from moving out of the simulation volume by zeroing the linear momentum of the base of the substrate at every timestep. Nose-Hoover style, non-Hamiltonian equations of motion were used in the isothermal-isobaric (NPT) ensemble (Ref 18) to perform the time integration with a time step of 0.001 ps (1 fs). This integrator also provided for the equilibration of the system to 300 K at an appropriate rate. Once the particle was set in motion, the canonical, energy conserving integrator (NVE) was used. A 1 fs timestep was used because the simulations converged using this timestep, and thus shorter timesteps that increase computational cost were not required.

Since most of the deformation occurred in the first few picoseconds after impact, the positions of all atoms and thermodynamic variables were recorded at intervals of 0.2 ps for 10 ps to study the dynamic deformation mechanisms that are responsible for the range of deformation behavior observed. Data files also included thermodynamic variables such as total potential energy (PE), total kinetic energy (KE), PE/atom, and KE/atom (proportional to atom temperature). The relaxation of the NP following impact (after 10 ps) was evaluated by capturing atomic positions at intervals of 50 ps for up to 800 ps after impact, stopping after the shape of the particle and its microstructure were no longer noticeably evolving. OVITO software (Ref 19) was used to visualize the atomic positions, and polyhedral template matching (PTM) (Ref 20) was used to determine the local atomic configuration. The visualizations were color-coded by PTM configuration, with green representing FCC and red representing HCP local atomic configuration, using a RMS deviation cutoff set to 0.15, which is within the guidelines for distorted crystals. When the atomic stacking sequence could not be identified (e.g., at grain

boundaries, surfaces, or where the atoms were disordered), atoms were identified as "other" and were colored gray. OVITO was also utilized to evaluate strain (von Mises local shear invariant and the volumetric strain) for the atoms in the NP. Dislocation identification utilized three methods: (1) dislocation analysis (DXA) in OVITO, (2) viewing the particle from different 3D views in OVITO, and (3) examining <110> views of the particle, as shown in Fig. 4 and 5.

From previous studies, it is known that the nucleation and motion of partial dislocations plays a large role in the deformation behavior of impacting NPs. (Ref 13) The Schmid factor (Ref 15) is a measure of the resolved shear stress acting on specific atomic planes in specific directions during application of a global stress, and therefore it is a quantifiable measure of the driving force for dislocation motion. In FCC systems, slip can occur along any of the four equivalent {111} planes and in any of the three equivalent <110> directions that lie in each {111} plane. Thus, there are 12 possible geometric slip systems. The Schmid factor was calculated for each NP impact direction for all 12 slip systems to determine if it is a useful tool in understanding Ag NP deformation. The Schmid factors were compared to the deformations experienced by the NPs upon impact. The magnitudes of the NP deformations were quantified from the measured particle aspect ratio, defined as the ratio of maximum width normal to the impact direction to maximum height parallel to the impact direction, which were obtained from the final state of the impacted particles.

First, three sets of simulations were conducted to span the possible NP orientations with respect to a fixed z [001] substrate. In these simulations, the NP diameter was 4.5 nm and the impact velocity was 300 m/s. The first set started with the NP and substrate in the same orientation with commensurate lattices; this was defined as the reference orientation. The three sets of simulations were conducted with the impacting NP rotated from the reference orientation about: (1) the z axis, (2) the y axis, and (3) multiple axis rotations that aligned the impact axis of the NP with selected indexed crystallographic directions. First, the NP was rotated about the z [001] axis at 5° intervals up to a maximum misorientation of 45°. The symmetry of the system dictates that rotations larger than 45° duplicate the rotations within 0-45°. For the second set of simulations, the impacting NP was rotated about the y [010] axis at 5° intervals up to a rotation angle of 45° where the impact axis was [101]. Note that for rotations about the y [010] axis, there is a different impact axis for each rotation. For the third set of simulations, the NP was impacted at specific orientations obtained from a standard triangle in the stereographic projection. The impact axes were two successive rotations about the z and y axes of the original NP



orientation, and this set of rotations included the [111] impact direction. Collectively, the simulated impact directions spanned the unique region within the stereographic projection.

Further simulations were conducted in which the NP diameter was 4.5, 6, or 9 nm, and impact velocities were selected to span from little deformation (300 m/s) up to cases where the entire NP final state was found to be epitaxial with the substrate (1200 m/s for 4.5 and 6 nm, and 1500 m/s for 9 nm). Impacting NP orientations were chosen at the corners of the unique stereographic projection: impact directions of [001] rotated 45° about the z axis of the substrate, [111], and [101].

A typical atomic cross section of the simulation volume before impact is shown in Fig. 1(a), where a 4.5 nm NP is rotated  $45^{\circ}$  about the z axis and viewed in a <110> direction, and both the NP and substrate are oriented with z [001]. A schematic of an impacted particle on a substrate and the variables needed to evaluate the deformation parameters are shown in Fig. 1(b). This figure illustrates the width and height of the deformed particle used in quantifying the aspect ratio.

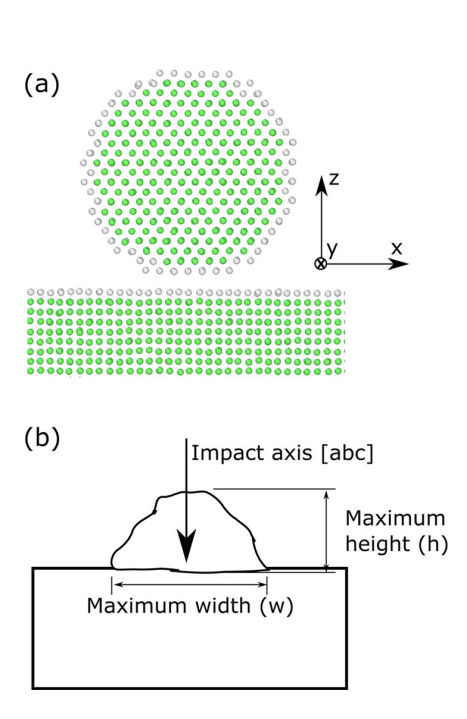


**Fig. 1** (a) Cross-section image of a whole 4.5 nm NP and substrate before impact. This impacting NP orientation has Miller indices (in the simulation box): x [110], y [ $\overline{1}$  10], z [001]; i.e., a 45° rotation about the z axis. The substrate orientation has Miller indices: x [100], y [010], z [001]. (b) Schematic of the NP and substrate following impact showing the variables needed to evaluate the aspect ratio

### Results of Simulations

# **Testing Hypotheses that Deformation is Correlated** with Schmid Factor or Elastic Coefficients

One possible hypothesis is that the deformation of the impacting NP may be correlated with the elastic stiffness of the NP as given by its directional elastic modulus. For FCC silver, the elastic modulus is minimum in the [100] (44 GPa), is maximum in the [111] (120 GPa), and is intermediate in the [101] (84 GPa, a local maximum in the x-y plane). For comparison, the aspect ratios after NP impact of 4.5 nm NPs at 300 m/s are displayed in Fig. 2(a) in a stereographic projection. At the index directions at the four corners, the aspect ratio is 1.69 at [001] 0°, 1.72 at [001]45°, 1.15 at [111], and 1.18 at [101]. The deformation is minimum for both the [111] and [101] impact directions, and thus, does not agree with the intermediate elastic modulus in the [101] direction. This confirms that the magnitudes of the observed deformations are not correlated with the magnitude of the elastic moduli.

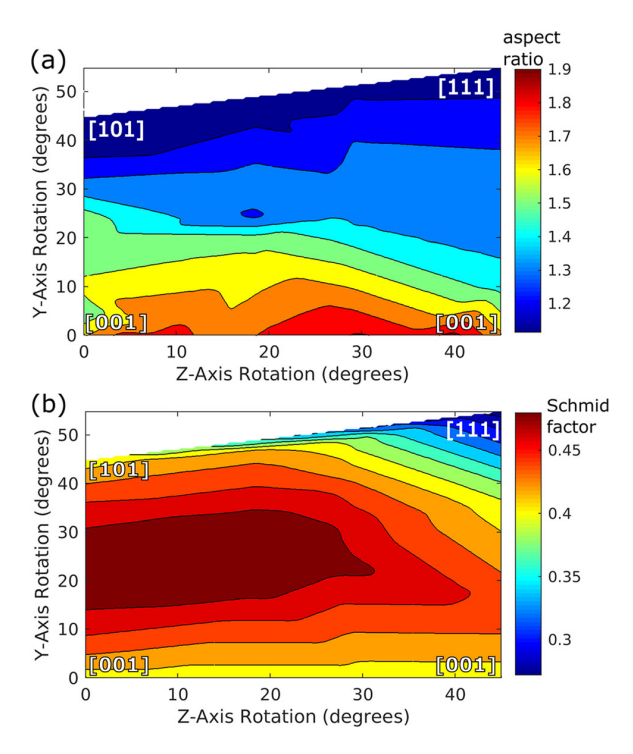


**Fig. 2** (a) Final aspect ratios for 4.5 nm particles incident at 300 m/s as a function of initial particle orientation prior to impact. The axes show rotations of the NP about the z and y axes to obtain the particle orientation prior to impact; the origin on this plot is the substrate orientation z [001], and the rotations are with respect to this axis. (b) Calculated Schmid factors as a function of NP rotations about its initial z and y axes. The numbers in brackets on the plots are the Miller indices for specific indexed impact directions



An alternative hypothesis is that the permanent deformation is correlated with the direction in which slip is favored (largest Schmid factor) with respect to the vector force of the impact. To test this hypothesis, the calculated Schmid factors are plotted as a function of the rotation axes of the impacting NP in the stereographic projection of Fig. 2(b). This figure shows that the directions having the lowest Schmid factors in the NP lie along the trace connecting the [111] and [101] directions (top edge of Fig. 2b), and they are lowest nearest the [111]. The highest Schmid factors appear when the impact axis is rotated such that it has a 20-25° rotation about the y [010] axis. The Schmid factors remain high for 20-25° rotation about the y [010] axis for simultaneous rotations about the z [001] from 0° up to about 30° (dark brown band at the left center of Fig. 2b). It is in this band of high Schmid factors, where the maximum value is 0.498, that the deformation is predicted to be highest. To the contrary, Fig. 2(a) shows, the highest deformation is observed when the impact axis is aligned along [001], which also includes NP rotations about [001], and only modest deformations are obtained in directions where the Schmid factor predicts the highest deformations. The lowest deformation is observed for NPs with their impact axis aligned along the trace between the [111] and [101], which is only partly consistent with predictions based on the Schmid factor analysis. The minimum Schmid factor is in the [111] direction at 0.272, but it is at a relatively high value in the [101] direction at 0.408, and it varies monotonically along the trace between these two directions. Thus, although there is some correlation between directions where the calculated Schmid factors and measured aspect ratios are both small, the Schmid factor analysis fails to predict the directions where large deformations are observed.

The trend is for aspect ratio to be greatest for the soft impact orientation [001] rotated 45° with respect to the substrate (hereafter denoted as [001]r). It is somewhat smaller for incidence along the [111], smallest along the hard direction [101]. These trends continue for NP diameters and impact velocities that span the range of variables tested as shown in Fig. 3. The plot shows final aspect ratios for example cases of diameters and velocities for three of the corner Miller indices, [001]r, [111], and [101]. The lack of agreement between the aspect ratio following impact with either Young's modulus or Schmid factor persists. In the simulations, [101] remains the hard direction with [111] intermediate and [001]r soft.

The above analysis suggests that the underlying deformation mechanisms that are responsible for the range of deformation behaviors observed as a function of particle orientation are complex and require more detailed analysis. Additional simulations that encompass the extremes of deformation behavior, which correspond to the three

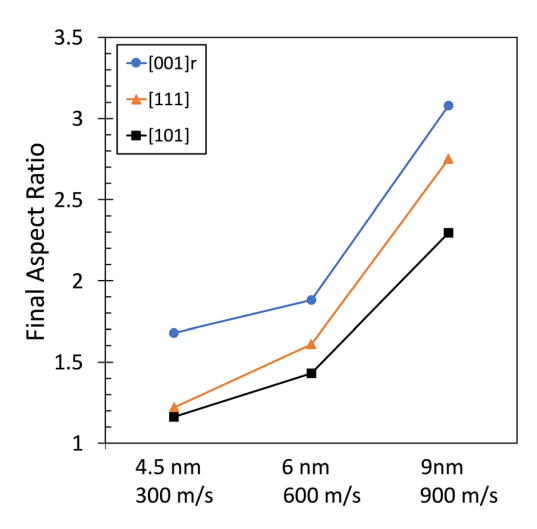


**Fig. 3** Final aspect ratio vs. particle diameter for example cases that span all three diameters and all three corner Miller indices of Fig. 2. Impact velocities are as noted on the horizontal axis. (A complete set of data points for aspect ratio vs. impact velocity are shown later in Fig. 9 collected at the time of maximum particle deformation.)

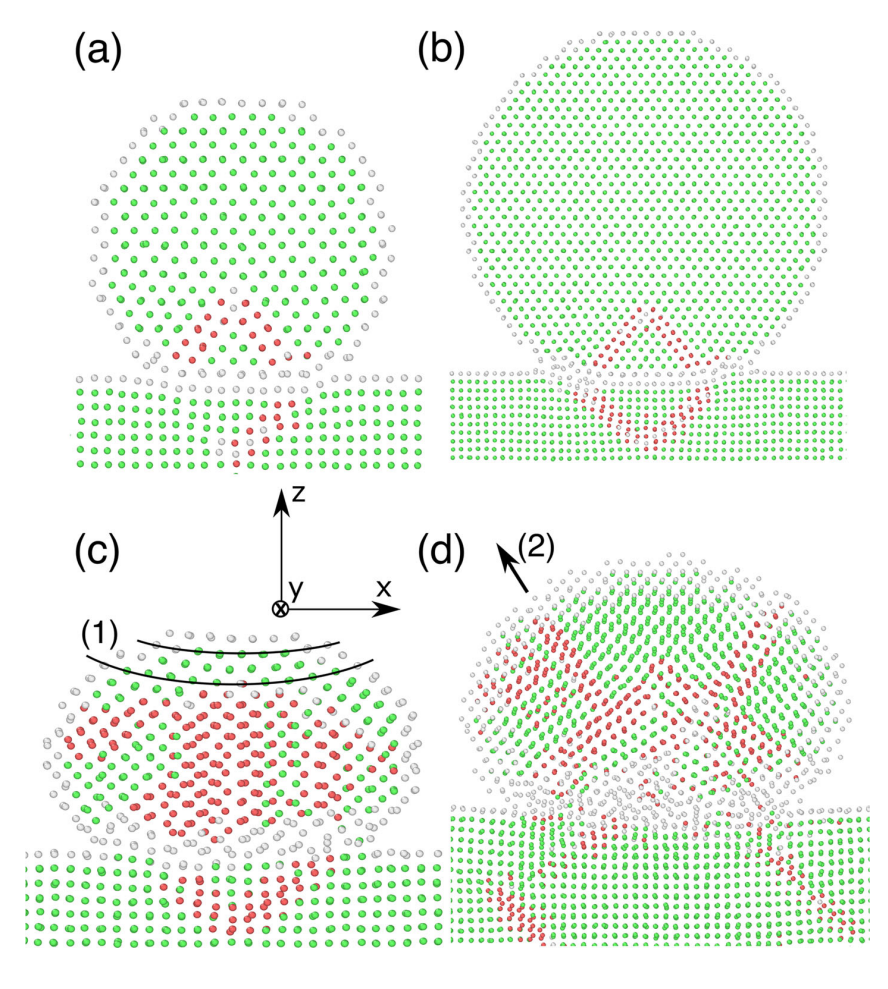
particle orientations [001]r, [111], and [101], were therefore studied to further understand the deformation mechanisms that are responsible for the range of deformations in the impacted NPs.

#### **Deformation Mechanisms for Soft Orientation**

Example simulations are shown in Fig. 4 for soft impacts of [001]r-oriented 4.5 nm particles at 300 m/s and 9 nm particles impacted at 600 m/s. These cases span the range of diameters and are at sufficiently low impact velocities to emphasize the initial mechanism, i.e., easily visible partial dislocations, versus disordering. For all subsequent atom images where the atomic configuration is encoded by PTM, green represents FCC atomic configuration, red represents HCP (stacking faults produced by the motion of partial dislocations), and gray represents 'other' atoms that could not be categorized as a defined crystal structure and therefore are presumed to be disordered. A careful examination of the dislocations in Fig. 4(a) and (b) shows Shockley partial dislocations being emitted from the edges of the contact zone between the particle and substrate that propagate on non-coplanar {111} planes into the NP. These partial dislocations intersect, resulting in a pyramid-like feature comprised of stacking faults that are at angles of  $\pm 35^{\circ}$  relative to the impact direction (in this <110> view of the NP). Their intersection produces a Lomer-Cottrell lock which prevents further motion of the intersecting partial dislocations. (Ref 21) At these early time steps, deformation is highly localized to the pyramidal region. As the NP continues to move downward, the



Fig. 4 Cross section atom views during particle impact showing the evolution of the microstructure of a [001]roriented NP impacting on a flat [001] substrate: (a) 4.5 nm NP, 300 m/s at 1.2 ps after impact (0.5 nm thick section), (b) 9 nm NP 600 m/s at 1.0 ps after impact (0.7 nm thick section), (c) 4.5 nm NP, 300 m/s at 4.1 ps after impact (0.7 nm thick section, 0.4 nm off center) where (1) denotes reference curves that highlight curved atomic planes, and (d) 9 nm NP, 600 m/s at 4.6 ps after impact (0.9 nm thick section, 3.5 nm off center) where (2) denotes the propagation direction of a typical Shockley partial that has propagated to the surface



contact area between the particle and substrate expands, leading to additional partial dislocations that nucleate from the edges of the expanding contact zone and propagate parallel to the initial partial dislocations. It has been shown previously that this pyramidal feature acts like a rigid wedge as the upper part of the NP continues to move downward onto the nearly stationary pyramid. (Ref 13) As material is pushed aside by motion onto the pyramid, the horizontally oriented {001} planes above the pyramid are bent about the pyramid apex (see Fig. 4c and d), and the upper part of the NP is spread apart. To accommodate the severe strains that accumulate locally in the region above the pyramid apex, additional partial dislocations nucleate from the pyramid apex and propagate outward toward the NP surface following {111} planes. Since the angles of the {111} planes vary due to deformation of the particle, the dislocation angles vary as they follow the local orientations of {111} planes. The atoms near the boundary between the particle and substrate disorder upon impact. This disordered zone does not grow substantially following impact at these lower impact velocities. There are more gray atoms in the 9 nm particle impacting at 600 m/s, and they are located at the substrate interface and in irregular regions in the NP, particularly near the center where a number of dislocations have merged. The number of atoms in the different atomic configurations will be quantified in a following section. Similar dislocation behavior to that described here for 4.5 and 9 nm NPs is also observed in simulations of 6 nm particles impacted at 600 m/s.

It is apparent that partial dislocation motion is not limited to the impacting particle, but also occurs into the substrate. The resulting substrate plastic deformation accommodates some of the deposited energy. Following impact, the elastic strains are recovered, and the partial dislocations can either retreat to the surface or trailing partial dislocations nucleate that combine with the leading partial dislocations and disappear to relax the imposed strains in the substrate. Either of these scenarios will eliminate stacking faults, and with rare exceptions, return the substrate lattice to a defect-free final state. A similar observation is apparent in the NP where the density of partial dislocations decreases with time, but unlike the



substrate, some partial dislocations are observed in the particles in their final state, especially if the final state is not epitaxial.

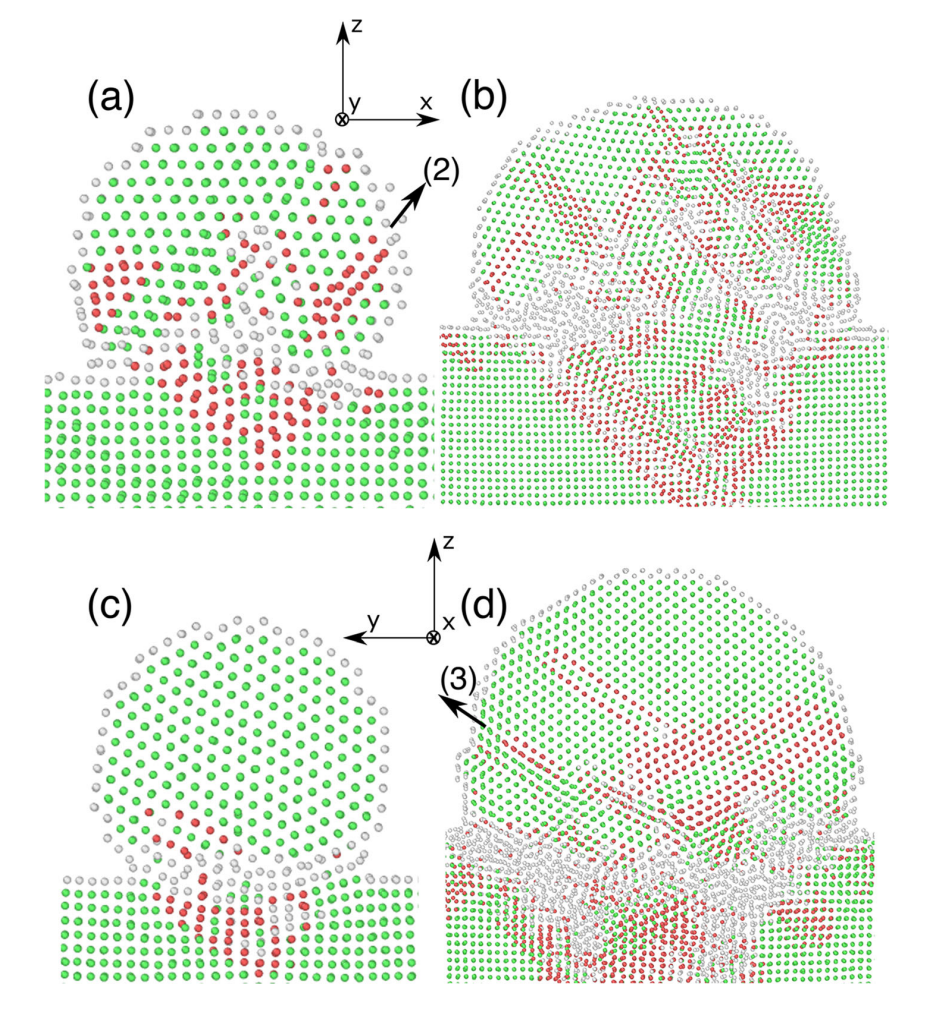
#### **Deformation Mechanisms for Hard Orientations**

For NP impact along the [111], the impacting NP is oriented with Miller indices: x [11 $\overline{2}$ ], y [ $\overline{1}$  10], z [111]. Figure 5(a) and (b) show the microstructure of the NP-substrate system following impact for 4.5 nm NPs at 300 m/s and 9 nm NPs at 600 m/s. As was observed for the soft impact orientation, the deformation upon impact is initially localized near the contact region. Due to the relative orientations of the impact axis and the close-packed, inclined {111} planes where dislocations propagate, the pyramidal feature observed for the soft orientation is not observed for this case. However, the lattice misorientation between the NP and the substrate still produces a relatively highly stressed contact region that results in the nucleation and propagation of partial dislocations in {111} planes in

both the substrate and NP. It is also notable that the {111} planes in the upper regions of the NP, parallel to the substrate surface in this case, do not bend as they did for the soft impact orientation. This is because the pyramidal feature is not present. As the NP continues moving downwards, the contact area expands, leading to the nucleation and propagation of partial dislocations on {111} planes that originate at the contact surface and terminate at the upper NP surface (Fig. 5a and b). As the NP stops moving, the propagating partial dislocations reach the NP surface. Notable in this case is that the dislocations move to the top of the NP at relatively steep angles following {111} planes, and thus the entire NP contains defects.

For NP impact along the [101], the impacting NP is oriented with Miller indices: x [10 $\overline{1}$ ], y [010], z [101]. Figure 5(c) and (d) show the microstructure of the NP-substrate system following impact for 4.5 nm NPs at 300 m/s and 9 nm NPs at 600 m/s. During the initial stages of impact, the deformation is localized near the contact area with partial dislocations nucleating from this zone as

Fig. 5 Cross section atom views during particle impact showing the evolution of the microstructure of: (a) a [111]oriented 4.5 nm NP, 300 m/s at 4.5 ps after impact (0.5 nm thick section) where (2) denotes the propagation direction of a typical Shockley partial that has propagated to the surface, (b) a [111]-oriented 9 nm NP 600 m/ s at 7.6 ps after impact (0.9 nm thick section), (c) a [101]oriented 4.5 nm NP, 300 m/s at 2.5 ps after impact (0.5 nm thick section), and (d) a [101]oriented 9 nm NP, 600 m/s at 6.4 ps after impact (1.5 nm thick section) where (3) denotes the propagation direction of a typical Shockley partial that is still in motion toward the surface





was observed in the previous [111] orientation simulation. However, in this case the partial dislocations in the NP propagate nearly horizontally (Fig. 5c and d) rather than upwards. This occurs because slip is occurring in the most favorably oriented {111} planes, where the shear stress is highest. Most of the deformation in this case is concentrated in the lower half of the NP, and the upper regions of the NP retain their pre-impact crystal orientation. Similar to the previous cases, the motion of partial dislocations into the substrate results in deformation in the substrate that is recovered at longer time steps.

#### **Atom Classifications Versus Time**

The behaviors shown for the three NP orientations in Fig. 4 and 5 are summarized in Fig. 6-8 by quantifying the changes in the number of atoms classified in the three PTM configurations versus time. Figure 6-8 show the PTM changes for particles with diameters of 4.5, 6, and 9 nm, respectively. Each figure contains data for impacts at 300, 600, and 900 m/s for all three impact orientations and extends to just past the time of maximum deformation. The physical significance of these times is that they are long enough so that most of the changes in atomic configurations due to deformation have stabilized and relaxation processes have begun.

First, examine the decrease in number of FCC atoms over time for the three orientations. For all three impact velocities shown in Fig. 6, the minimum in the percentage of FCC atoms is lowest for the soft particle orientation [001]r. The minimum in the percentage of FCC atoms is higher for the [111] orientation and highest for the hard orientation [101]. This trend of the softest orientation [001]r having the greatest percentage of atoms transform out of the FCC configuration is maintained in Fig. 7 and 8. The only exception to this behavior is noted in the top row of Fig. 8 for 9 nm particles impacting at 300 m/s where the [111] orientation is minimum at -18.5% FCC atoms and the [101] orientation is minimum at -22.3% FCC atoms. This [111] case is marked at several times by the visible disappearance of partial dislocations containing HCP atoms in the NP, which leaves an undisturbed FCC lattice. One of these instances of atoms converting from HCP to FCC configuration is also visible at  $\sim 8$  ps in the time dependence of FCC and HCP percent as an inflection that represents a reversal of the trend of increasing HCP atoms with time. For all the cases, the atoms that no longer are classified as having an FCC configuration transform to either an HCP configuration or other. How the atoms are distributed between these two configurations varies with time and with the other parameters.

A second observation based on Fig. 6-8 is that the percent of HCP atoms is most significant at lower impact velocity, e.g., 300 and 600 m/s for 9 nm NPs in Fig. 8. As

impact velocity increases, the percent of other atoms overtakes the percent of HCP atoms, and in most cases the percent of HCP atoms peaks before the time of maximum deformation and maximum percent of other atoms.

A third observation is that, for a given impact velocity, the percent of HCP atoms increases with particle diameter. This is particularly noticeable for 300 m/s impacts of 4.5 and 6 nm particles (Fig. 6 and 7, respectively) where the percent of HCP is equal to or less than the percent of other atoms for 4.5 nm particles, but the percent of HCP atoms is greater than or equal to the percent of other atoms for 6 nm particles. This same behavior is visible for 600 m/s impacts when comparing 6 and 9 nm diameter particles in Fig. 7 and 8.

In summary, the decrease in the overall deformation or aspect ratio of the NP is associated with a corresponding decrease in transitions of atoms away from FCC configuration. This decrease in aspect ratio as the impact behavior proceeds from soft to hard orientations corresponds to [001]r, [111], and [101] particle orientations. At lower impact velocities and at earlier times, transitions to HCP configuration are generally greater than or equal to the transitions to other; however, as impact velocity increases, transitions to the disordered configuration dominate. Both the creation and propagation of dislocations and the viscous flow of disordered atoms contribute to the deformation of the NP. The smaller deformation for the two harder orientations can be attributed in part to the absence of the rigid, wedge-like pyramidal feature, that formed from the intersecting {111} planes in the soft orientation. This wedge produced significant deformation throughout the particle, and the upper half of the NP was severely strained. The primary mechanisms for limited deformation observed for harder orientations can be attributed to favorably oriented {111} planes for the [111] particle orientation where the shear stress can propagate dislocations throughout the NP. For the [101] particle orientation, the {111} planes are less favorably oriented and so the dislocations remain confined to the lower half of the NP and the upper half is not significantly strained. As the impact velocity increases, a larger percentage of atoms disorder, and this disorder spreads from the substrate-NP interface and from regions with high defect concentrations.

# Dependence of Particle Aspect Ratio on Impact Velocity and Particle Diameter

The aspect ratio was measured at times where it had stabilized at approximately its maximum value: 4, 8, and 10 ps for 4.5, 6, and 9 nm diameter particles, respectively. These times also correspond to the approximate times where the number of disordered atoms reaches its maximum. Measuring these parameters consistently at these times eliminates annealing effects that occur at later times so that the



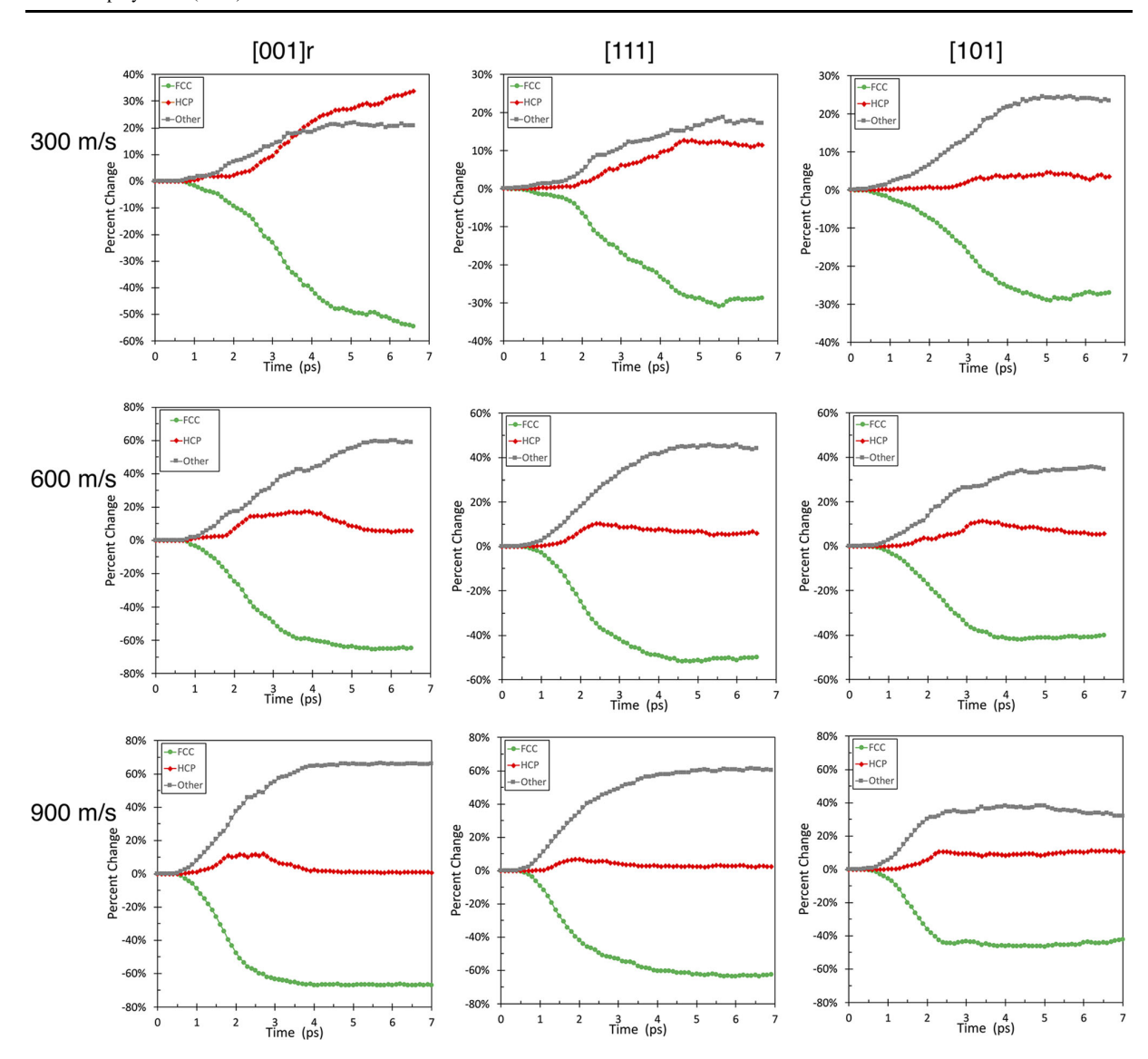


Fig. 6 Percent change in number of atoms in the impacting particle identified by PTM as FCC, HCP, and other vs. time for 4.5 nm particles. Velocity in rows: 300, 600, and 900 m/s, descending. Orientation in columns: [001]r, [111], and [101], left to right

aspect ratio at maximum deformation can be compared to the percent of disordered atoms. Care was taken to measure the particle height by including atoms contained in the particle that lie below the substrate surface level, and the data are plotted in Fig. 9. A trend of increasing aspect ratio as particle orientation goes from the hard [101] to the soft [001]r orientation is observed, similar to that seen for the larger decrease in the percent of FCC atoms going from hard to soft. The difference in aspect ratio for the different particle orientations is quite clear; however, there is comparatively little variation in aspect ratio with particle diameter from 4.5 to 9 nm. Comparing Fig. 9 to Fig. 6-8, it is apparent that there is a correlation between a large aspect ratio (e.g., large particle

deformation) and the percentage of atoms that transformed from the FCC configuration. Large aspect ratios are achieved whether the atoms convert from FCC to a mixture of HCP and other or to primarily other; for example compare Fig. 8 (600 m/s, [001]r) and Fig. 6 (600 m/s, [001]r).

# Spatial Correlation of Defected and Disordered Atoms, PE/Atom, and Shear Strain per Atom

We begin this analysis by dividing the particles into groups of atoms according to several variables related to the state of the atoms and use this information to analyze deformation during NP impacts. Motivation for this approach is



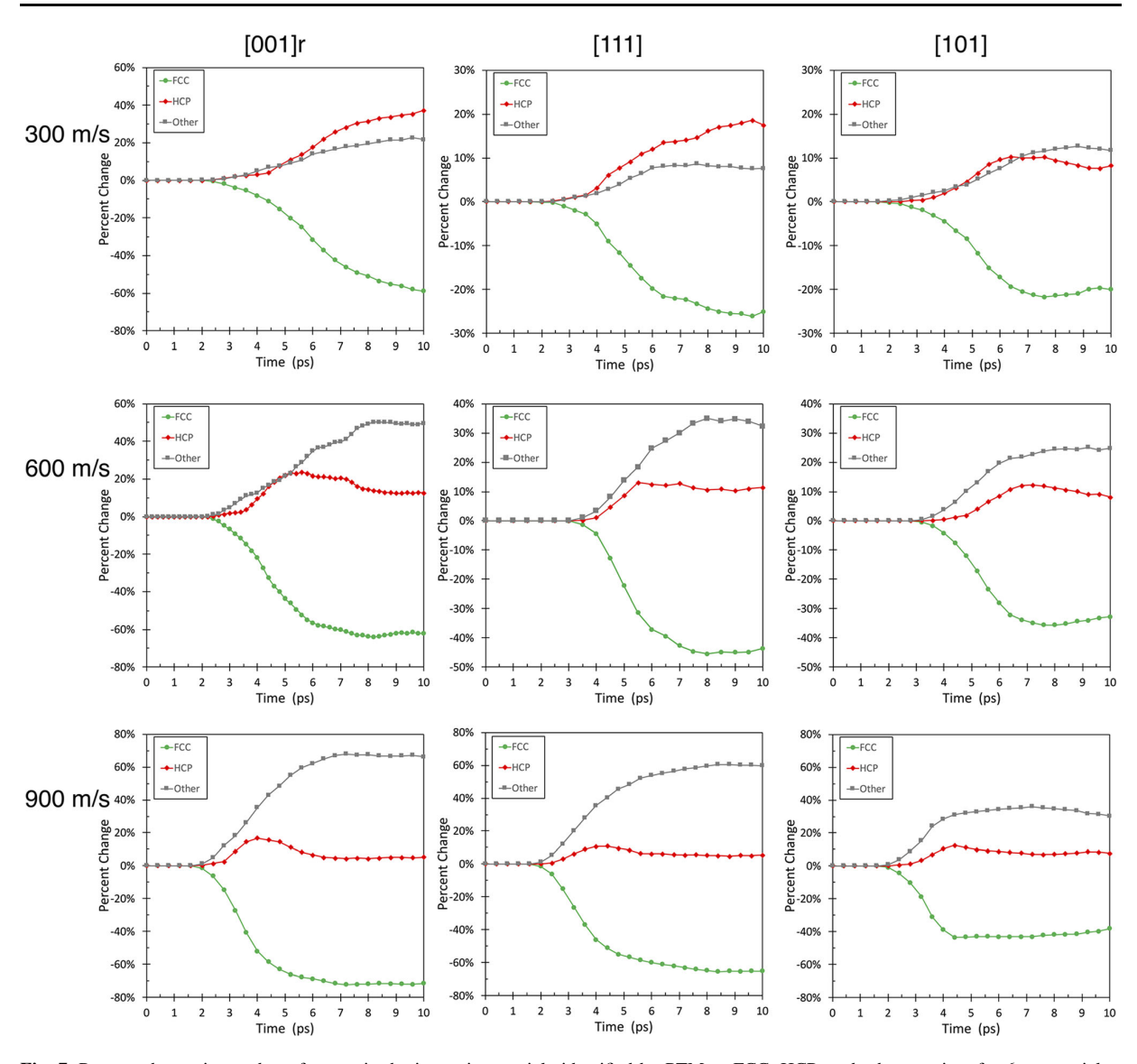


Fig. 7 Percent change in number of atoms in the impacting particle identified by PTM as FCC, HCP, and other vs. time for 6 nm particles. Velocity in rows: 300, 600, and 900 m/s, descending. Orientation in columns: [001]r, [111], and [101], left to right

provided in Fig. 10 that displays  $\sim 1.5$  nm thick cross sections of the three NP impact orientations for 4.5 nm particles at 300 m/s sampled at 4 ps. At this time, the number of other atoms and the aspect ratio are all near their peak values. The figures are color coded in rows by PTM configuration (top), PE/atom (middle), and shear strain (bottom). The PE/atom variable allows us to eliminate surface atoms from the analysis using a threshold of -2.5 eV since they have a much higher PE/atom than the rest of the atoms. For color coding, a threshold is set at the measured disorder threshold of -2.70 eV (red) for Ag atoms. (Ref 22-24) Thus, the red atoms in Fig. 10(d) and (f) are either surface atoms or are atoms that are likely to

disorder. In addition, each row in Fig. 10 can be compared vertically to the other rows to search for similar patterns among the three variables for a given orientation. For example, note the similarity in the locations of the gray regions of other atoms in the top row, the red regions of high PE/atom in the second row, and lastly, the regions of high shear strain (orange to red) in the bottom row. This suggests separating atoms within the NPs by PTM configuration to examine whether there is a correlation between shear strain and disordered or defected atoms. This hypothesis will be explored in detail in the next section where the relative contributions of dislocation plasticity and viscous flow to shear strain will be quantified.



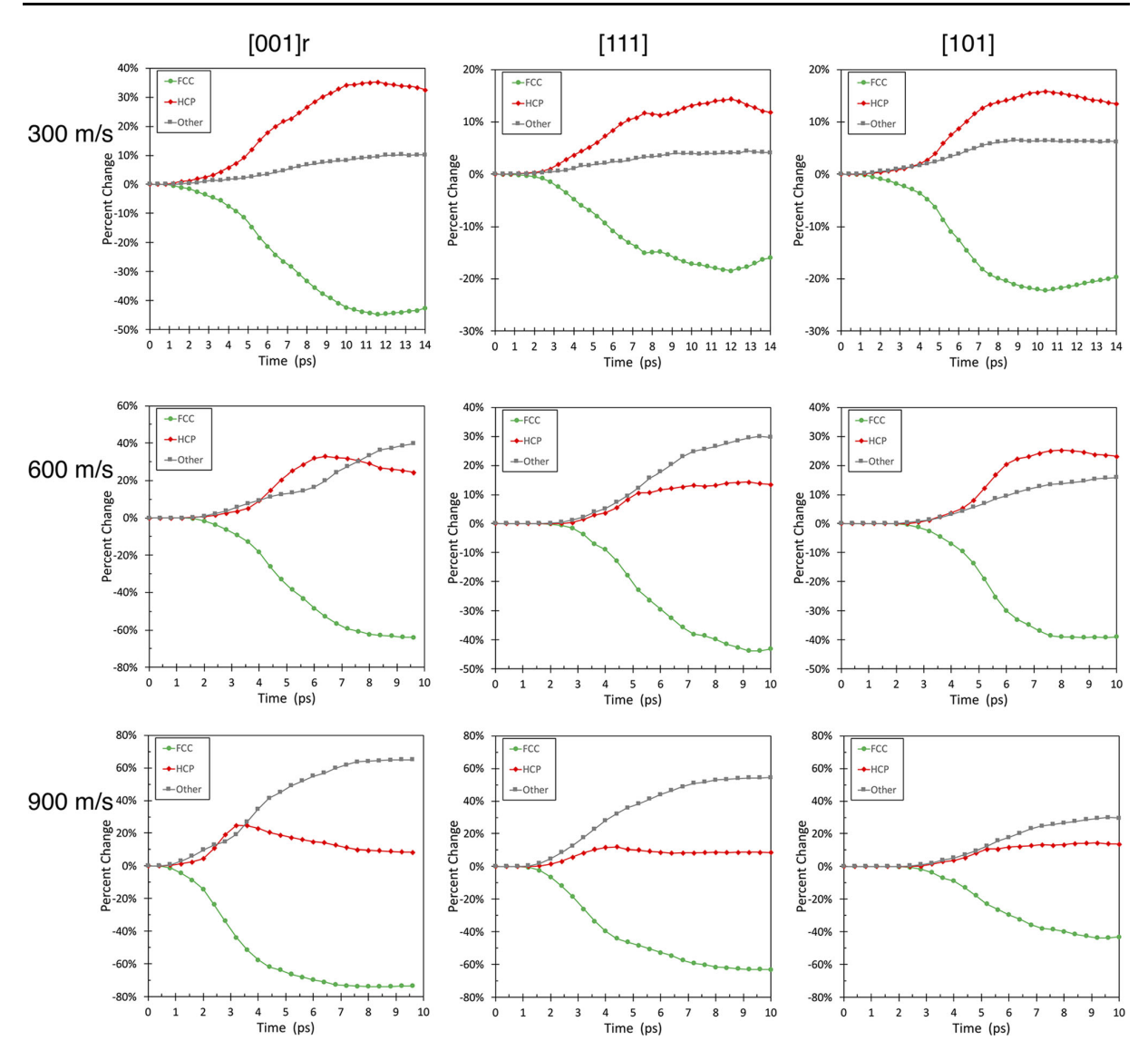


Fig. 8 Percent change in number of atoms in the impacting particle identified by PTM as FCC, HCP, and other vs. time for 9 nm particles. Velocity in rows: 300, 600, and 900 m/s, descending. Orientation in columns: [001]r, [111], and [101], left to right

# Contribution to Shear Strain by Local Atomic Configuration (PTM)

In this section, we determine the contributions to the total particle deformation from dislocation motion and from viscous flow for each particle orientation. This is done by examining the orientation dependence by PTM configuration of: (1) the percent of atoms in each configuration, (2) the average shear strain per atom for that configuration, and (3) the *total* shear strain contribution of the atoms in each configuration, which is defined as the product of the previous two quantities (with % of atoms divided by 100). For a particular PTM configuration, the product of strain per atom and the fraction of the total atoms in that

configuration is particularly meaningful. It represents the contribution to the total strain weighted by each of the PTM configurations. The sum of these products over the three configurations is equal to the average strain per atom for the entire particle. Consistent with the previous analyses, these comparisons are all done at the approximate time of maximum deformation.

The percent of atoms associated with deformation resulting from dislocation motion is indicated by the percent of HCP atoms. The percent of atoms that are disordered and can deform by viscous flow are indicated by those with the PTM configuration other. We hypothesize that these two groups of atoms together can contribute to deformation roughly in proportion to their numbers.



Figure 11 and 12 show the effectiveness of the various groups of atoms' contribution to overall strain and particle

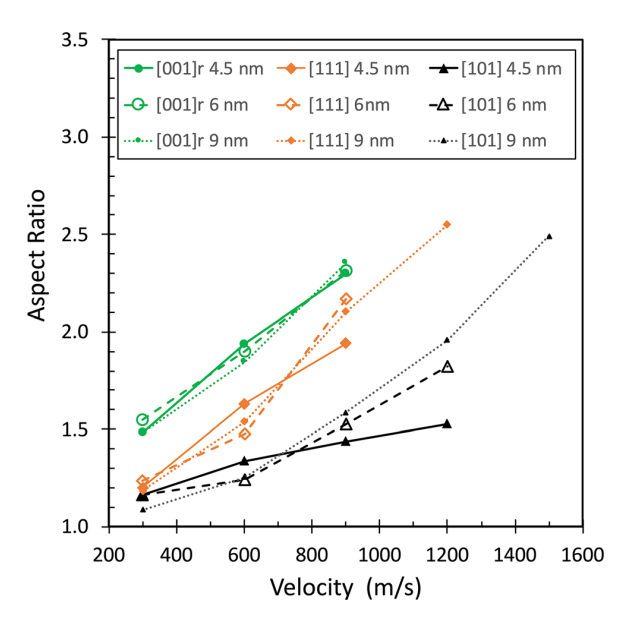
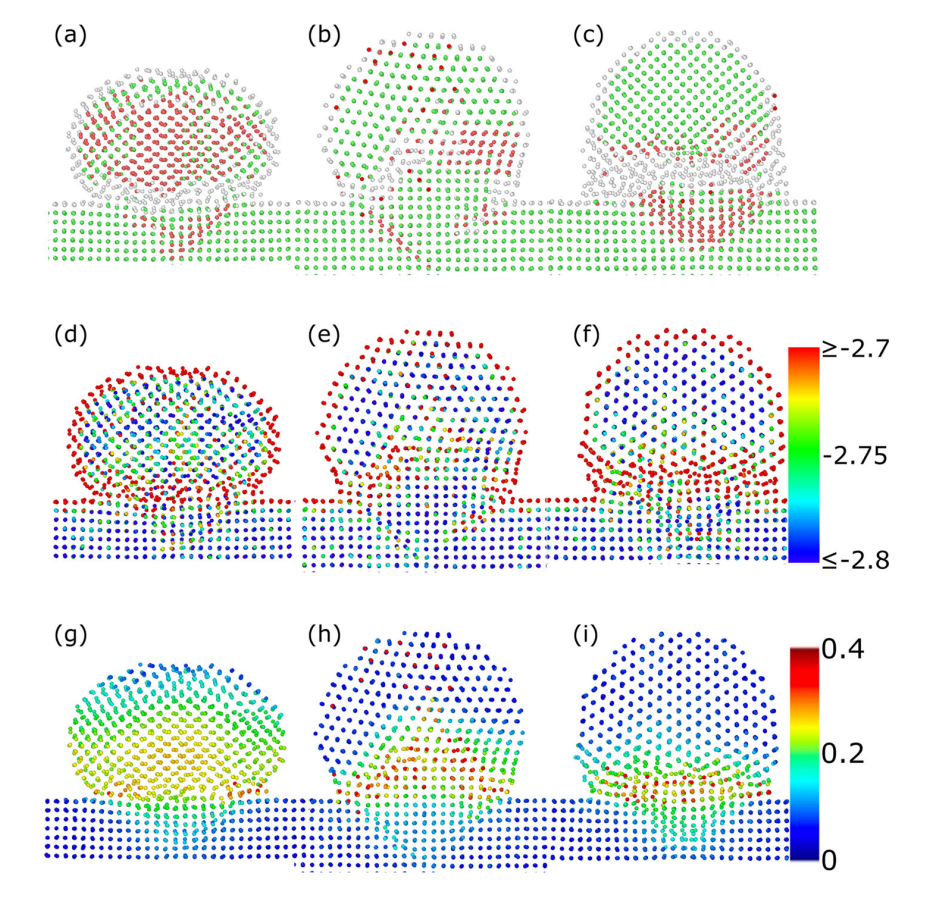


Fig. 9 Aspect ratio vs. impact velocity for all NP sizes and the three indexed orientations

Fig. 10 Cross sections ( $\sim 1.5$  nm thick) of 4.5 nm NPs impacted at 300 m/s viewed in the <110> direction for all three indexed orientations at 4 ps after impact. (a-c) PTM classification of atoms with green = FCC, red = HCP, and grey = other; (d-f) PE/atom with blue = -2.8 eV and red = -2.7 eV; and (g-i)cumulative shear strain with blue = 0 and red = 0.4(referenced to t = 0). Left column NP impact orientation is [001]r; middle column orientation is [111]; and right column orientation is [101]

deformation. Figure 11 breaks down the data for 4.5 nm particles by orientation and by PTM configuration for percent of atoms in the group (left column), average strain per atom in the group (center column), and the product of the previous two for each group (right column). The right column is a graphical representation of the contribution by the atoms in each PTM configuration to total particle shear strain. The data spans impact velocities from 300 to 900 m/s. The same format is used in Fig. 12 for 9 nm particles. The data for 6 nm particles closely resembles that for 9 nm particles and is shown in the Supplemental Materials.

Several important observations can be made regarding Fig. 11 and 12. For impact at 600 and 900 m/s, disordered atoms make by far the largest contribution to shear strain and thus deformation via viscous flow. At 300 m/s impact velocity for the soft orientation, [001]r, strain via HCP atoms that identify dislocation plasticity is larger than the strain contribution of the disordered atoms. For the two harder orientations at 300 m/s, [111] and [101], the contribution to the total strain from disordered atoms is slightly larger or about the same as for the contribution from dislocation plasticity. This correlates with the previous observation that, except for the two cases of impact at 300 m/s for 4.5 and 6 nm, [001]r particles, HCP atoms





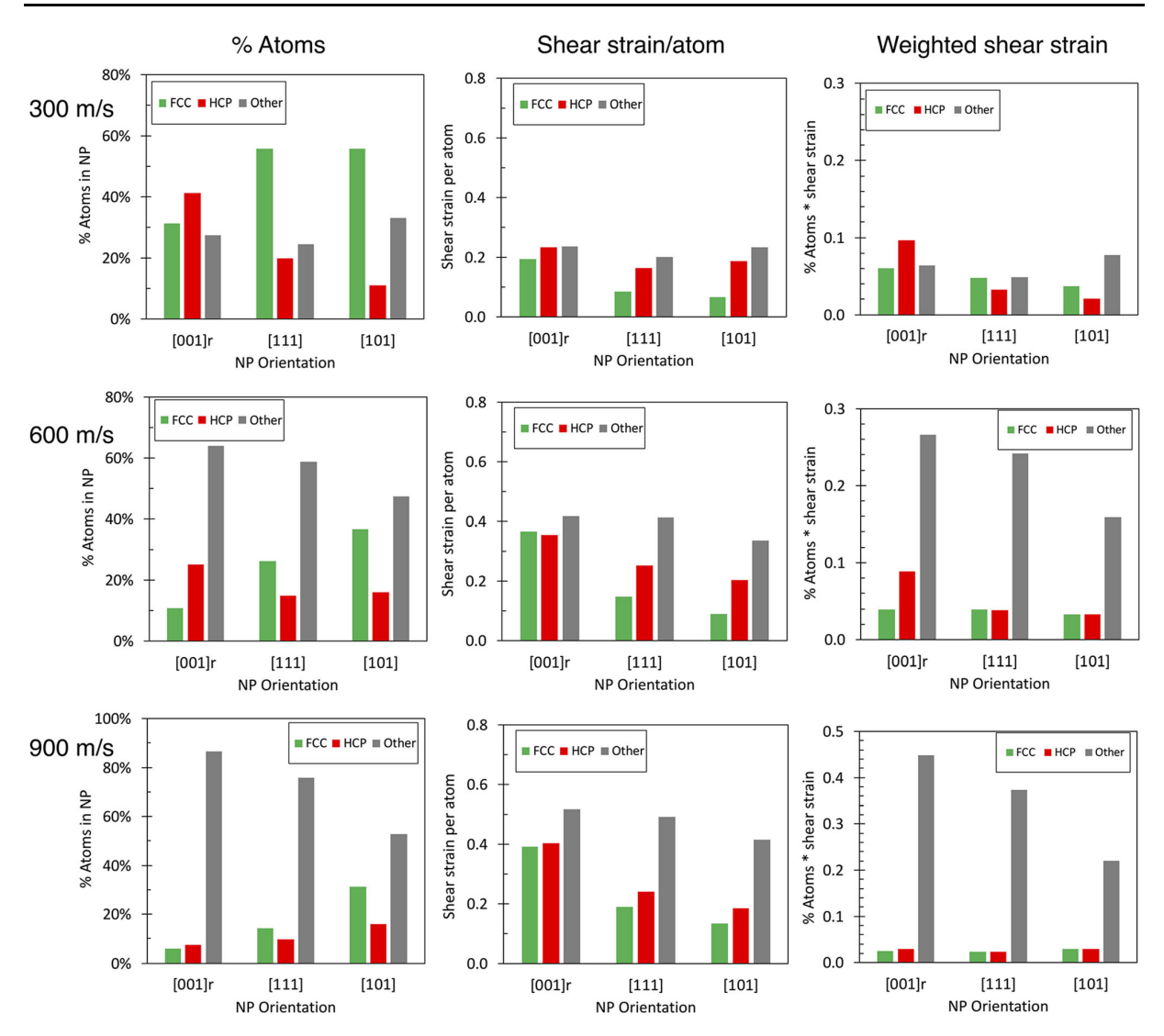


Fig. 11 Percent of atoms in PTM configurations FCC, HCP, and other for the three particle orientations (left column), shear strain per atom (center column) by atomic configuration and orientation, and contribution to total shear strain (product of the strain per atom and

percent of atoms) by atomic configuration and orientation (right column). All cases are 4.5 nm particles at the approximate time of maximum deformation and at impact velocities of 300 m/s (top row), 600 m/s (second row), and 900 m/s (bottom row)

peaked and began to decrease in numbers before peak deformation of the particle was reached.

The dominance of disordered atoms' contribution to shear strain cannot be explained by their superior strain per atom as shown in the center column of Fig. 11 and 12. Their strain per atom is only slightly larger than the contribution of the HCP atoms. Instead, the large contribution of the disordered atoms results from their larger numbers, particularly for larger velocities and softer orientations where deformation is greatest. When the number of disordered atoms is not large, their contribution to strain via viscous flow is comparable to the contribution by atoms exhibiting dislocation plasticity.

Finally, it is notable that differences in deformation mechanisms for different particle orientations first arise by differences in dislocation motion in {111} planes. Although the number of atoms classified as HCP shrinks and their role in deformation is overtaken by disordered atoms as deformation progresses, the orientational differences in deformation classed as "hard" or "soft" persist for higher velocity impacts even where viscous flow eventually dominates.

# Conditions for Final State to be Epitaxial

After the point of maximum deformation and maximum number of disordered atoms, there is a period of relaxation to



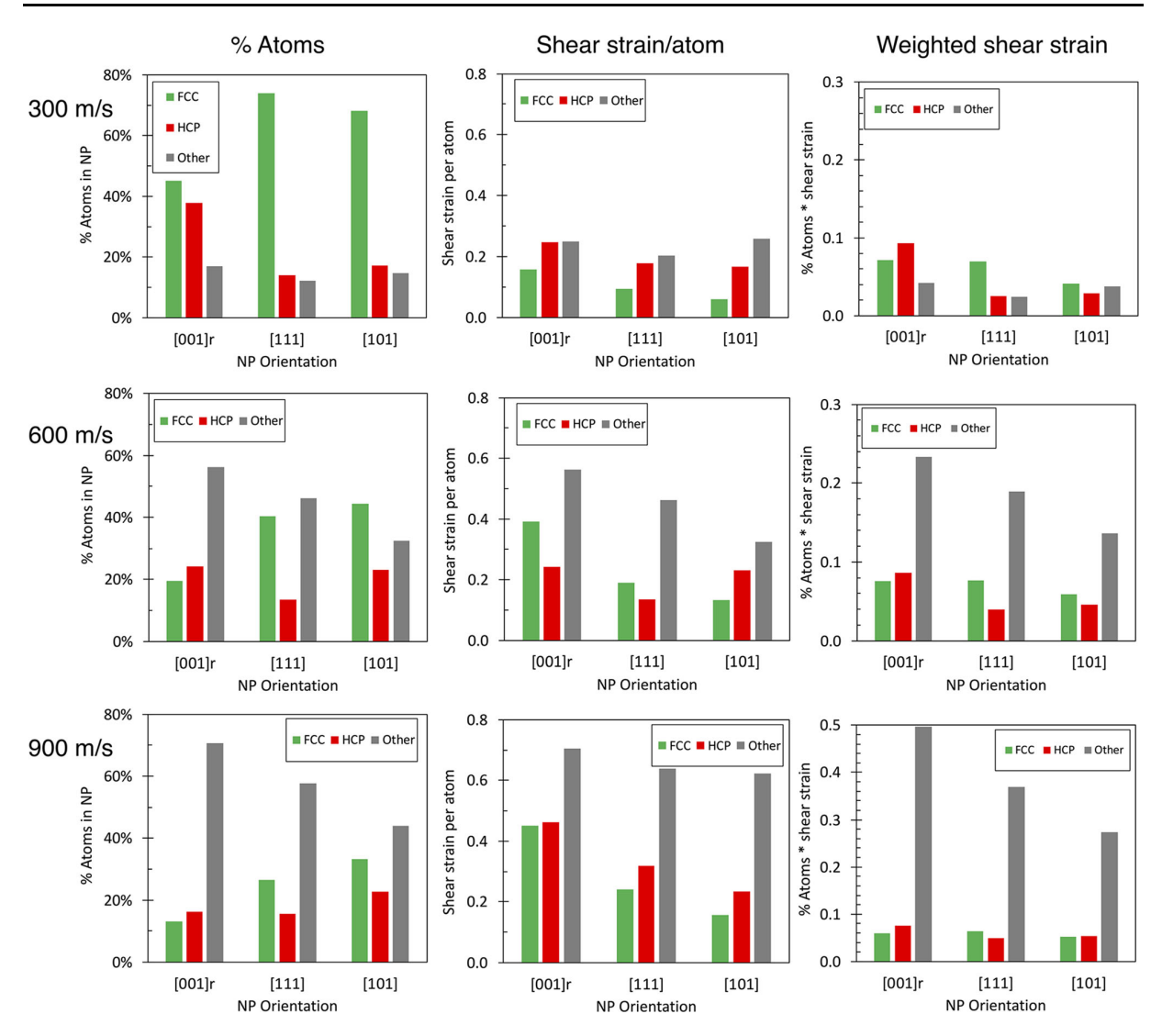


Fig. 12 Percent of atoms in PTM configurations FCC, HCP, and other for the three particle orientations (left column), shear strain per atom (center column) by atomic configuration and orientation, and contribution to total shear strain (product of the strain per atom and

percent of atoms) by atomic configuration and orientation (right column). All cases are 9 nm particles at the approximate time of maximum deformation and at impact velocities of 300 m/s (top row), 600 m/s (second row), and 900 m/s (bottom row)

a final state lasting up to about 0.5 ns. Without detailed examination of the various regrowth and relaxation mechanisms, one can classify the final state of the system as being polycrystalline or epitaxial with the substrate. Answering three questions is central to this discussion. (1) Do particle orientation effects persist through the relaxation process? To answer this question, simulation experiments were conducted to answer a second, more specific question. (2) Which conditions for NP orientation, NP diameter, and impact velocity lead to epitaxy? A third question is suggested by previous work that tracked the final crystal state for [001]r oriented Ag particles as a function of diameter and velocity. (Ref 13) This work found that increasing disorder during

particle impact eventually leads to an epitaxial final state. So, a final question to be answered is: (3) Which is the better indicator of a final epitaxial state, maximum percent of disordered atoms or maximum deformation as measured by aspect ratio?

Simulations were conducted for all NP orientations and diameters for impact velocities ranging from 300 m/s up to a velocity that resulted in an epitaxial final state. The observed maximum percent of disordered atoms for each case is shown in Table 1. The heavy red line separates the polycrystalline final states (top) from the epitaxial final states (bottom). Two cases for 4.5 nm particles incident at 600 m/s and orientations [001]r and [111] ended epitaxial



with the substrate, but contained  $\sim 3$  thin stacking imperfections on the upper surface of the particle. These data clearly answer the first two questions. Orientation effects persist through to the final equilibrated state, and the conditions for epitaxy can be ascertained from Table 1.

To answer the third question, maximum particle aspect ratio was measured for the same cases in Table 1. These aspect ratio data (same as Fig. 7) are plotted on the horizontal axis in Fig. 13 versus the maximum percent of other atoms on the vertical axis. The raw data for aspect ratio are included in the Supplemental Materials in the same format as Table 1. Although aspect ratio and percent of other atoms are clearly correlated, it is clear that a percent of other atoms above 60-70% is required for epitaxy. For aspect ratio, there is a wider range of overlap between cases that end as polycrystalline and epitaxial. Thus, maximum percent of disordered atoms is the better indicator of the final crystalline state.

### Discussion

Our primary scientific objective is to determine the causes of orientation differences in the deformation of Ag particles as they impact. It has been previously established that both dislocation plasticity and viscous flow of amorphous atoms play a role in the deformation process. (Ref 13) In the present study, the effects of particle orientation on deformation were found to be not correlated with either the anisotropic elastic properties of Ag or to the favored slip direction(s) as predicted by the Schmid factor. Although Schmid factor predicts the initiation of {111} slip for a uniform, uniaxial strain, for particle impact, the orientation of slip planes changes after the initiation of dislocation plasticity, which changes the driving forces both for the nucleation of new dislocations as well as the propagation of dislocations after they nucleate. In addition, there are extremely strong gradients in the magnitude of the strains and the strain state is non-uniform. This combination of factors is likely responsible for the lack of correlation between the deformation observed in the MD simulations and the predictions from the Schmid factor analysis.

Orientation differences were found to be important in determining where and when dislocations initiate along {111} planes as shown in Fig. 4 and 5. For different particle orientations, the densities and locations of active {111} slip planes are distributed differently within particles of differing orientation owing to differences in strain and strain state with respect to slip directions. Simultaneously with dislocation plasticity, some atoms disorder at the particle-substrate contact surface and where the density of dislocations is high. Thus, there are contributions to deformation from both dislocation plasticity and viscous flow of disordered atoms for all particle orientations.

The particle aspect ratio is both a global measure of deformation and a direct measure of the relative hardness for a particular particle orientation. Aspect ratio decreases from softest to hardest orientations, [001]r, [111], and [101], respectively. For a given particle orientation, varying particle diameter from 4.5 to 9 nm has little effect on the final particle aspect ratio, indicating that the orientation effects are more significant than the particle size effects and that interaction effects between particle size and particle orientation are minimal in this particle size range.

Shear strain per atom was studied in relation to whether each atom was participating in deformation via dislocation plasticity or viscous flow. When atoms are classified according to their PTM configuration, HCP atoms are normally found to peak in number before the point of maximum particle deformation and then the number of HCP atoms begins to decrease, as shown in Fig. 6-8. At the same time, disordered atom numbers continue to increase and peak around the time of maximum deformation. When the contribution to shear strain is divided among defected and disordered atoms, their respective effectiveness and contribution to deformation can be obtained, as shown in Fig. 11 and 12. The dominance of disordered atoms' contribution to shear strain via viscous flow is not explained by their larger strain per atom. Their strain per atom is only slightly greater than the contribution of the HCP atoms via dislocation plasticity. Instead, the contribution of the disordered atoms results from their larger numbers, particularly for higher impact velocities and for softer particle orientations where deformation is greatest. Although the number of disordered atoms increases as impact velocity increases, and viscous flow dominates deformation, orientational differences that initiated earlier in the impact process persist and therefore are responsible for the observed anisotropy in plastic deformation.

As the impact process stabilizes, orientation effects are seen in the number of atoms that disorder. This is clearly demonstrated in Table 1 where all particle orientations become epitaxial if the impact velocity is sufficient. The final state correlates more closely with disorder percentage than it does with aspect ratio, as shown in Fig. 13. Orientation differences in anisotropic dislocation nucleation and atomic disorder that arise early in the impact event are seen to persist in the percent of disordered atoms and in the required percentage of disordered atoms sufficient for a final epitaxial state to occur. A general rule was hypothesized from the data in Fig. 13 that suggests that 60-70% of the atoms in the impacting particle becoming disordered is sufficient for the final state of the particle and substrate to be epitaxial. It is notable that 100% disordering is not required for an epitaxial final state. There are a myriad of processes that occur as the system stabilizes, which we have not studied in detail. However, the simulations have



**Table 1** Maximum percent of other atoms for all indexed orientations, sizes, and velocities (Color table online)

NP dia.				
4.5 nm	Indexed impact direction			
<i>V,</i> m/s	[001]r	[111]	[101]	
300	27.3%	24.4%	33.2%	
600	64.0%	58.6%	47.4%	
900	86.6%	75.9%	52.8%	
1200			68.8%	EPI
6 nm				
300	27.1%	20.2%	25.7%	
600	53.5%	36.3%	34.4%	
900	79.8%	69.9%	43.6%	
1200			71.1%	EPI
9 nm				
300	17.1%	12.1%	14.7%	
600	56.3%	46.2%	32.5%	
900	70.6%	57.8%	44.0%	
1200		73.2%	63.0%	
1500			74.2%	EPI

Thick, solid lines separate the cases with a final polycrystalline state from cases with a final epitaxial state. Cells at 4.5 nm and 600 m/s for [001]r and [111] are single crystal with several thin stacking imperfections on the surface

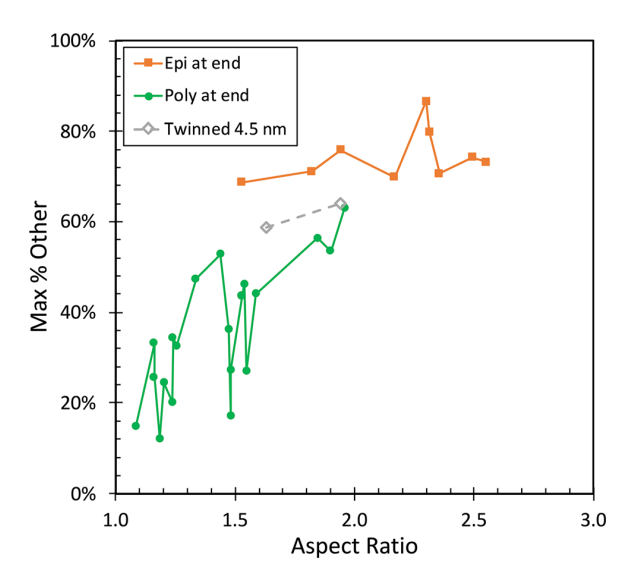
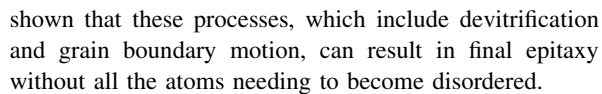


Fig. 13 Maximum percent of other atoms vs. aspect ratio with green circles indicating cases that finish as polycrystalline (poly) and orange squares indicating cases that finish epitaxial (epi). Two cases that are crystalline with several thin stacking imperfections on the NP surface are gray open diamonds



It was found that the orientational dependence on deformation that is initiated early in the impact process continues with the same ordering from soft to hard orientations through to the final state of the system. Early differences in nucleation of dislocations and disordering of atoms lead to differences in strain per atom due to different numbers of atoms participating in each of these deformation mechanisms. These differences eventually lead to different numbers of disordered atoms (for a given impact velocity) and finally to orientational differences in whether the final state becomes epitaxial.

#### Conclusions

We conducted MD simulations of spherical, single crystal silver nanoparticle impacts onto flat, crystalline silver surfaces. The range of variables studied was consistent with experimental deposition processes for Ag particles with diameters from 4.5 to 9 nm and impact velocities of 300 to 1500 m/s. Particle crystallographic orientations spanned the range of unique orientations. Three orientations were selected for detailed analysis because they exhibited the widest range of deformations. Particle orientation effects during the deformation process and on the final state of the system were the primary interest of this study.

Orientation differences in deformation are found to persist throughout the impact. These differences start with Shockley dislocations nucleating on {111} planes that are oriented differently for each particle impact orientation, and they grow at different rates depending on the strain and strain state in the deforming particle. At the same time, atoms at the impact interface and at high defect density locations become disordered. Thus, differing locations and numbers of defected and disordered atoms are generated depending on the particle orientation. From these deformation differences (differences in particle aspect ratio), hard and soft particle orientations are defined proceeding form soft to hard as [001]r, [111], and [101]. As a function of time, defected atom numbers increase and peak before maximum particle deformation, while disordered atom numbers increase to at least the time of peak deformation. Disordered atoms contribute more to strain per atom (particle deformation) by virtue of their larger numbers as compared to defected atoms. On a per atom basis, they both contribute roughly equally to strain.

After sufficient time for the particle and substrate to stabilize after impact, the final state of the system can be determined: polycrystalline or epitaxial. The same particle



orientation dependence for epitaxy is found where softer particle orientations, which deform more and have a larger percentage of disordered atoms, can epitaxy at a lower impact velocity. The impact velocity where epitaxy occurs is identified and depends on both particle size and particle orientation. The maximum percentage of disordered atoms is a good predictor of whether a particle will epitaxy; the results from the simulations suggest a threshold of at least 60-70% disordered atoms is required. These results show how orientation differences arise and that they persist through the impact event and extend to the final stabilized system state.

For the experimental deposition of Ag particles, orientation cannot be controlled. Our findings would be useful in setting experimental impact velocity where an aerosol of impacting particles would contain all possible orientations. For example, if a polycrystalline deposit is desired, a lower impact velocity can be selected. However, this case might be complicated since a small number of epitaxial impacts would only increase the grain size slightly, and our results do not speak directly to void formation. Conversely, if an epitaxial film is desired, a sufficient velocity should be selected such that all orientations become epitaxial.

**Supplementary Information** The online version contains supplementary material available at <a href="https://doi.org/10.1007/s11666-023-01664-5">https://doi.org/10.1007/s11666-023-01664-5</a>.

Acknowledgments This work was supported by the National Science Foundation under Grant No. CMMI 2102818. The authors acknowledge the Texas Advanced Computing Center (TACC) at The University of Texas at Austin for providing HPC resources that have contributed to the research results reported within this paper. URL: <a href="http://tacc.utexas.edu">http://tacc.utexas.edu</a>.

Availability of Data The data that support the findings of this study are available from the corresponding author upon reasonable request.

Competing interest The authors declare that they have no known competing financial interests or personal relationships that could have appeared to influence the work reported in this paper.

#### References

- S. Kashu, E. Fuchita, T. Manabe, and C. Hayashi, Deposition of Ultra Fine Particles Using a Gas Jet, *Jpn. J. Appl. Phys.*, 1984, 23, p. L910-L912.
- M. Oda, E. Fuchita, M. Tsuneizumi, S. Kashu, and C. Hayashi, Gas Deposition Films of Ultra Fine Particles, *Nanostruct. Mater.*, 1992, 1, p 203-206.
- W.T. Nichols, G. Malyavanatham, M.P. Beam, D.E. Henneke, J.R. Brock, M.F. Becker, and J.W. Keto, Synthesis of Nanostructured WC Films by Supersonic Impaction of Nanoparticle Aerosols, MRS Symp. Proc., 2000, 581, p 193-198.
- W.T. Nichols, D.T. O'Brien, G. Malyavanatham, M.F. Becker, and J.W. Keto, Supersonic Nanocrystal Deposition for Nanostructured Materials, MRS Symp. Proc., 2002, 703, p 209-214.

- C. Huang, W.T. Nichols, D.T. O'Brien, M.F. Becker, J.W. Keto, and D. Kovar, Supersonic Jet Deposition of Silver Nanoparticle Aerosols: Correlations of Impact Conditions and Film Morphologies, *J. Appl. Phys.*, 2007, 101, p 064902.
- M. Nahar, J.W. Keto, M.F. Becker, and D. Kovar, Highly Conductive Nanoparticulate Films Achieved at Low Processing Temperatures, *J. Electron. Mater.*, 2015, 44, p 2559-2565.
- J.J.H. McCallister, J.W. Keto, M.F. Becker, and D. Kovar, Influence of Normal Velocity on Microstructure and Density of Films Produced by Nanoparticle Impact, AIP Adv., 2019, 9(3), p. 035226.
- H. Haberland, Z. Insepov, M. Karrais, M. Mall, M. Moseler, and Y. Thurner, Thin Film Growth by Energetic Cluster Impact (ECI): Comparison Between Experiment and Molecular Dynamics Simulations, *Mater. Sci. Eng. B*, 1993, 19, p 31-36.
- H. Ogawa, Molecular Dynamics Simulation on the Single Particle Impacts in the Aerosol Deposition Process, *Mater. Trans.*, 2005, 46(6), p 1235-1239.
- J. Tarus and K. Nordlund, Molecular Dynamics Study on Si<sub>20</sub> Cluster Deposition on Si(0 0 1), Nucl. Instrum. Methods Phys. Res. B, 2003, 212, p 281-285.
- H. Zhu and R.S. Averback, Molecular Dynamics Simulation of Densification Processes in Nanocrystalline Materials, *Mater. Sci. Eng.*, 1995, A204, p 96-100.
- H. Jami and A. Jabbarzadeh, Unravelling Ultrafast Deformation Mechanisms in Surface Deposition of Titanium Nanoparticles, Appl. Surf. Sci., 2019, 489, p 446-461.
- T.V. Chitrakar, J.W. Keto, M.F. Becker, and D. Kovar, Particle Deposition and Deformation from High Speed Impaction of Ag Nanoparticles, *Acta Mater.*, 2017, 135, p 252-262.
- T.V. Chitrakar, G.J.J. Noiseau, J.W. Keto, M.F. Becker, and D. Kovar, An Experimental and Computational Study of High-Speed Impact of Ag Nanoparticles, J. Appl. Phys., 2019, 125, p 195104.
- W.D. Callister and D.G. Rethwisch, Materials Science and Engineering: An Introduction, Wiley, New York, 2010.
- 16. S. Plimpton, Fast Parallel Algorithms for Short-Range Molecular Dynamics, *J. Comput. Phys.*, 1995, **117**, p 1-19.
- P.L. Williams, Y. Mishin, and J.C. Hamilton, An Embeddedatom Potential for the Cu-Ag System, *Model. Simul. Mater. Sci. Eng.*, 2006, 14(5), p 817-833.
- W. Shinoda, M. Shiga, and M. Mikami, Rapid Estimation of Elastic Constants by Molecular Dynamics Simulation Under Constant Stress, *Phys. Rev. B*, 2004, 69(13), p 134103.
- A. Stukowski, Visualization and Analysis of Atomistic Simulation Data with OVITO—The Open Visualization Tool, *Modelling Simul. Mater. Sci. Eng.*, 2010, 18, p 015012.
- P.M. Larsen, S. Schmidt, and J. Schiøtz, Robust Structural Identification via Polyhedral Template Matching, *Model. Simul. Mater. Sci.*, 2016, 24(5), p 055007.
- D. Hull and D.J. Bacon, Introduction to Dislocations, 5th ed. Butterworth-Heinemann, Oxford, 2011.
- M.F. Becker and D. Kovar, A Quantitative Criterion for Predicting Solid-State Disordering During High Strain Rate Deformation, *J. Phys. Condens. Matter*, 2020, 33(6), p 065405.
- M.F. Becker and D. Kovar, A Quantitative Criterion for Predicting Solid-state Disordering During Biaxial, High Strain Rate Deformation, *Model. Simul. Mater. Sci.*, 2021, 30(1), p 015006.
- T.V. Chitrakar, M.F. Becker, and D. Kovar, A Quantitative Criterion to Predict Atomic Disordering During High Velocity Nanoparticle Impact, *J. Aerosol Sci.*, 2022, 165, p 106042.

**Publisher's Note** Springer Nature remains neutral with regard to jurisdictional claims in published maps and institutional affiliations.



Springer Nature or its licensor (e.g. a society or other partner) holds exclusive rights to this article under a publishing agreement with the author(s) or other rightsholder(s); author self-archiving of the

accepted manuscript version of this article is solely governed by the terms of such publishing agreement and applicable law.

